Continuous Parametrisation of Wing Movable Layout for Design Optimisation

de Boer, S.; Sodja, J.; De Breuker, R.

Publication date
2024

Document Version
Final published version

Published in
Aeroelasticity & Structural Dynamics in a Fast Changing World 17 – 21 June 2024, The Hague, The Netherlands

Citation (APA)
de Boer, S., Sodja, J., & De Breuker, R. (2024). Continuous Parametrisation of Wing Movable Layout for Design Optimisation. In *Aeroelasticity & Structural Dynamics in a Fast Changing World 17 – 21 June 2024, The Hague, The Netherlands* Article IFASD 2024-57

Continuous Parametrisation of Wing Movable Layout for Design Optimisation

de Boer, S.; Sodja, J.; De Breuker, R.

Publication date
2024

Document Version
Final published version

Citation (APA)
de Boer, S., Sodja, J., & De Breuker, R. (2024). *Continuous Parametrisation of Wing Movable Layout for Design Optimisation*. Paper presented at International Forum on Aeroelasticity and Structural Dynamics, Den Haag, Netherlands.

International Forum on Aeroelasticity and Structural Dynamics
IFASD 2024
17-21 June 2024, The Hague, The Netherlands

CONTINUOUS PARAMETRISATION OF WING MOVABLE LAYOUT FOR DESIGN OPTIMISATION

Stefan de Boer[1], Jurij Sodja[1], Roeland De Breuker[1]

[1]Delft University of Technology
Kluyverweg 1, 2629HS Delft, The Netherlands
S.deBoer-2@tudelft.nl
J.Sodja@tudelft.nl
R.DeBreuker@tudelft.nl

Keywords: Movables, Doublet Lattice Method (DLM), B-spline, Aeroelasticity

Abstract: In line with recent advancements in aviation, which lead to more fuel-efficient aircraft, this paper presents a novel continuous movable parameterisation methodology. The methodology takes advantage of the ability of the doublet lattice method (DLM) to describe aerodynamic forces using downwash. The movables are described in the continuous space using a downwash distribution generated using a B-spline surface. To demonstrate and assess the movable modelling methodology, the U-HARWARD aircraft model has been used, with the performance of the continuous parameterisation compared to a reference movable parameterisation for roll control, manoeuvre load alleviation and cruise performance. The results show that the continuous parameterisation can determine a downwash distribution that is at least equal in performance – during roll – or has better performance – for manoeuvre load alleviation and cruise performance – than the reference parameterisation. The continuous parameterisation showed a 3 percentage points improvement with respect to the reference parameterisation for manoeuvre load alleviation and a 2.4 percentage points improvement for the induced drag coefficient. The results in the paper demonstrated the successful application of a movable parameterisation methodology, which can be applied to an aircraft for which only the planform and initial structural parameters are known.

1 INTRODUCTION

Recent advancements in aviation, combined with the desire to develop more fuel-efficient aircraft, have led to more flexible aircraft designs, which can be accounted for with tailored structural design or active control such that the desired aerodynamic shape is achieved without unwanted aerodynamic-structure couplings. Using active control, the wing movables can be used for control, drag minimisation, load alleviation, and shape control such that the performance of the aircraft is improved throughout the flight envelope [1].

Examples of works applying active control to improve the aircraft's performance throughout the flight envelope using conventional movables are the works by Sanghi et al. [2–4], Riso et al. [5] and Ma et al. [6] who focused on the influence of aileron positioning on handling qualities (HQs). Pusch et al. [7], and Muradas et al. [8] investigated the effect of the movable layout on load alleviation capabilities. Furthermore, Wunderlich and Siebert investigated using the trailing edge movables to improve cruise flight performance [9].

The works presented above improved the aircraft's performance throughout the flight envelope; however, the authors were limited by the optimised cruise wing shape, which cannot be

optimised for the whole flight envelope because of conflicting structural and control requirements [10, 11]. Therefore, instead of fighting the flexibility of the aircraft structure, embracing it and changing the wing shape actively over the whole flight envelope using continuous movables would be more natural, such that the performance gap between the optimal configuration and the current cruise configuration can be reduced [12].

Continuous movables can be split into two main groups. The first group are morphing concepts, such as the VCCTEF concept [13–15] developed initially at NASA and the SmartX concept developed at TU Delft [11, 12, 16] who investigated the effect of continuous movables on load alleviation capabilities, drag minimisation and shape control. The second group is the use of distributed discrete movables along the trailing edge whose only degree of freedom is the deflection angle [17, 18], where Stanford investigated the use of distributed movables for load alleviation and flutter suppression. Both conventional and continuous movables can be used for drag minimisation, load alleviation and shape control.

The works mentioned considered wings containing fuel, limiting the design space available to the wing movables. Using different fuels, such as hydrogen, does not allow for fuel storage in the wing; hence, a dry wing is created, which increases the available design space. This paper will present a novel parameterisation methodology for wing movables, which uses B-splines to describe the movables in the continuous space and has been inspired by the shape functions used by Binder et al. [19, 20], that can be used to explore the expanded design space.

To show the functioning of the novel parameterisation methodology, the U-HARWARD aircraft model [21, 22] will be used to demonstrate and assess the movable parameterisation methodology, where roll capability, manoeuvre load alleviation (MLA) performance and cruise performance are considered. For comparison, the continuous parameterisation is applied to the same chordwise and spanwise extend as a reference parameterisation consisting of ailerons and flaps.

The paper has the following structure. First, section 2 discusses the aerodynamic modelling and novel continuous parameterisation methodology. section 3 discusses the framework built to apply the continuous parameterisation methodology in an optimisation process to determine the required movable layout. This is followed by section 4, which discusses the design problem to which the movable parameterisation methodology is applied. The results from the optimisation problem discussed in section 4 are presented in section 5, after which concluding remarks are given in section 6.

2 CONTINUOUS MOVABLE DESCRIPTION

This section discusses the novel parameterisation methodology proposed for describing the movables. First, the modelling method is presented, after which the continuous parameterisation methodology is explained.

2.1 Aerodynamic movable modelling

Several different methods are available to model movable aerodynamics, such as empirical listings of the lift and moment coefficients for a known deflection angle [23, 24], the unsteady vortex lattice method (UVLM) [25, 26], the doublet lattice method (DLM) [7, 27], or the use of computational fluid dynamics (CFD) [28, 29].

All of the methods presented have different pros and cons. For example, the empirical listing is very fast but only works for known movable dimensions. In contrast, CFD simulations allow

for different movable sizes and include nonlinear flow effects such as separation, but they are computationally expensive. Finally, UVLM and DLM can model movables of different sizes, but neither can account for flow separation. In the end, DLM was chosen, as it determines the loads using downwash, which can be directly assigned to the control points.

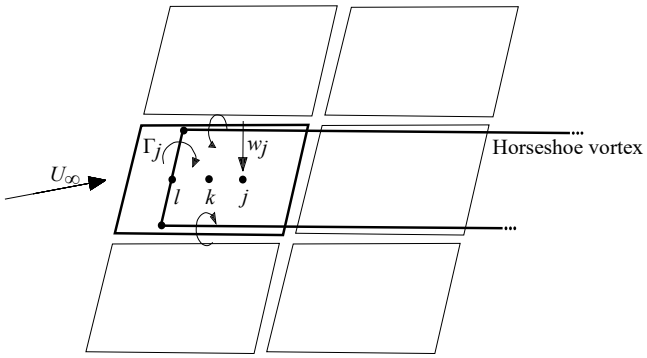

Figure 1: DLM mesh with different control points (l, k, j). Adapted from [27].

To apply DLM, the lifting surfaces of the aircraft are discretised using a set of trapezoidal panels, as shown in Figure 1, which have their control point j located at the three-quarter point. By applying the flow tangency condition at the control point j, the component of the flow normal to the panels $\mathbf{v}_j$ can be determined, which is normalised by the free-stream velocity U_∞ to create the downwash $\mathbf{w}_j$ as presented below [7, 27].

$$\mathbf{w}_j = \frac{\mathbf{v}_j}{U_\infty} \tag{1}$$

As a result of the DLM, the steady aerodynamic loads can be determined using the downwash at each control point,

$$\mathbf{P}_k^{\text{a, s}} = q_\infty \mathbf{S}_{kj} \mathbf{AIC} \left(\mathbf{w}_{j,\text{rbm}} + \mathbf{w}_{j,\text{cs}} + \mathbf{w}_{j,\text{uf}} + \mathbf{w}_{j,\dot{\text{u}}\text{f}} + \mathbf{w}_{j,\text{cam}} \right) \tag{2}$$

where q_∞ is the dynamic pressure, $\mathbf{S}_{kj}$ is the aerodynamic integration matrix, $\mathbf{AIC}$ is the aerodynamic influence coefficient (AIC) matrix. The terms in the $()$ represent different sources of downwash, where $\mathbf{w}_{j,\text{rbm}}$ is the downwash due to rigid body motion, $\mathbf{w}_{j,\text{cs}}$ is the downwash due to control surface deflection. Furthermore, downwash is also caused by flexible structural deformations, $\mathbf{w}_{j,\text{uf}}$, and flexible structural motion $\mathbf{w}_{j,\dot{\text{u}}\text{f}}$. Finally, the camber and twist of the airfoils also cause downwash, $\mathbf{w}_{j,\text{cam}}$, which needs to be incorporated in the force calculation [27].

The steady aerodynamic forces, $\mathbf{P}_k^{\text{a, s}}$, allow for trimming of the aircraft and manoeuvre-related loads such as pull-up, push-down or roll. To be able to perform gust analyses or take unsteady aerodynamic effects into account, both the gust force $\mathbf{P}k^{\text{a, g}}$ and the unsteady aerodynamic forces $\mathbf{P}k^{\text{a, us}}$ need to be added to the steady aerodynamic forces to get the total aerodynamic forces seen by the aircraft.

$$\mathbf{P}_k^{\text{a}} = \mathbf{P}_k^{\text{a, s}} + \mathbf{P}_k^{\text{a, g}} + \mathbf{P}_k^{\text{a, us}} \tag{3}$$

Equations (2) and (3) shows that the interesting component for movable allocation is

$$\mathbf{P}_k^{\text{a, cs}} = q_\infty \mathbf{S}_{kj} \mathbf{AIC} \mathbf{w}_{j,\text{cs}}. \tag{4}$$

As both the aerodynamic integration matrix $\mathbf{S}_{kj}$ and the AIC matrix $\mathbf{AIC}$, are functions of the panel discretisation applied to the aircraft, they can be considered constant throughout the aeroelastic performance assessment. Therefore, the downwash of the movables $\mathbf{w}_{j,\text{cs}}$ is a parameter which can be assigned to every panel.

2.2 Continuous movable modelling

For discrete movables, downwash due to control surface deflections is determined as follows. All DLM panels inside the movable region get assigned the same downwash value $w_{\text{j, cs}}$ for a deflection angle u_x, with the downwash value being calculated using

$$\mathbf{w}_{j,\text{cs}} = \left(\mathbf{D}^1_{jk} + s\frac{c_{\text{ref}}/2}{U_\infty}\mathbf{D}^2_{jk} \right) \mathbf{\Phi}_{kx}\mathbf{u}_x. \tag{5}$$

In this equation, the differentiation matrices $\mathbf{D}^1_{jk}$ and $\mathbf{D}^2_{jk}$ are used to transform the box movements and displacements from the reference point k (centre of the DLM panel) to a downwash at the control point j ($^3/_4c$ point of the panel) [30]. Matrix $\mathbf{D}^1_{jk}$ relates the steady displacement $\mathbf{u}_k$ at the reference point k to the local downwash velocity $\mathbf{w}_j$, with $\mathbf{D}^2_{jk}$ doing the same for the motion of the reference point $\dot{\mathbf{u}}_k$, with the movable mapping matrix $\mathbf{\Phi}_{kx}$ mapping the deflections of movables to the movement of individual aerodynamic boxes associated with the movable [30]. Furthermore, s denotes the Laplace variable, the reference chord is denoted by c_{ref}, and U_∞ is the free-stream velocity [7].

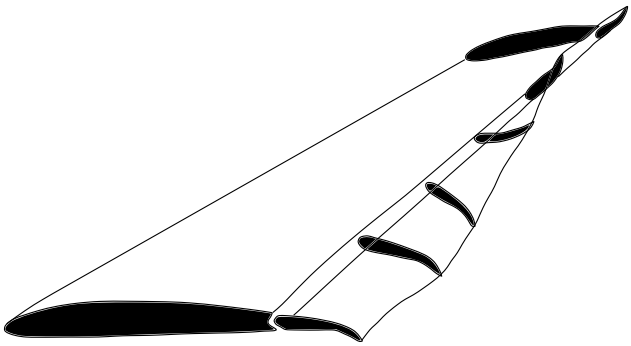

Figure 2: Continuous movables. Morphing in spanwise and chordwise directions. Adapted from Mkhoyan et al. [31].

However, when using continuous movables, which can morph in both chordwise and spanwise directions, as shown in Figure 2, the above methodology may not be able to model the behaviour of the continuous movables. For example, a continuous movable can show reflex behaviour in the chordwise direction as presented in Figure 3, where the downwash is not constant throughout the movable region. Using B-splines allows for the smooth description of different geometric shapes. However, instead of using the B-splines to describe the deformed shape of the continuous movable, we propose a novel application that describes the movables' downwash in the continuous space using B-spline surfaces.

The downwash distribution is defined using:

$$\mathrm{w}^{\text{cs}}(x, y) = \sum_{i=0}^{m}\sum_{l=0}^{n} N_{i,p}(x)\, N_{l,q}(y)\, \mathbf{p}_{i,l} \tag{6}$$

where $\mathbf{p}_{i,l}$ is a set of control points, and $N_{i,p}(x)$ and $N_{l,q}(y)$ are the B-spline basis functions of degree p and q respectively [32].

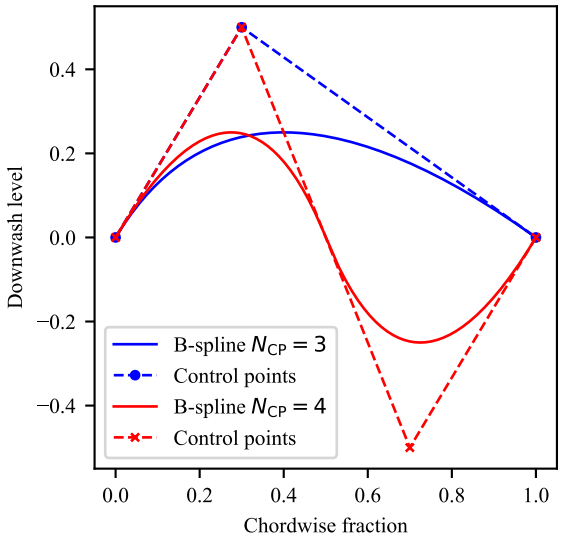

Figure 3: Reflex aerofoil: Comparison between three and four chordwise B-spline control points

The B-spline basis functions are generated using the Cox-de Boor recursion formula:

$$N_{i,0}(x) = \begin{cases} 1 & \text{if} \quad x_i \leq x < x_{i+1} \\ 0 & \text{otherwise} \end{cases} \tag{7a}$$

$$N_{i,p}(x) = \frac{x - x_i}{x_{i+p} - x_i} N_{i,p-1}(x) + \frac{x_{i+p+1} - x}{x_{i+p+1} - x_{i+1}} N_{i+1,p+1}(x) \tag{7b}$$

where the x_i are the knots inside the knot vector $\mathbf{X}$. The knot vector $\mathbf{X}$ is a set of parameters which determine how and where the control points influence the B-spline curve. For the basis function $N_{l,q}(y)$, the procedure shown in Equation (7) is also followed, however, in this case the y_l inside the knot vector $\mathbf{Y}$ and the degree q are used [32].

The degree p and q are one less than the order of the curve; furthermore, the number of control points must be equal to or greater than the order of the curve. For the modelling of the downwash distribution, a second-degree basis function is used in both the spanwise y and chordwise x directions, leading to a set of cubic curves using which the downwash distribution is generated. The second order for p and q was chosen as this is one of the most commonly used orders and has fast computation times [32, 33].

The downwash distributions are determined using a control point grid created on the wing. The corresponding downwash distribution is order two in the span- and chordwise directions, with the knots distributed uniformly over the downwash distribution. After the generation of the downwash distribution, the downwash, $w_{j,\text{cs}}$, at each panel is determined by evaluating the downwash distribution at the downwash control point j:

$$w_{j,\text{cs}} = \mathrm{w}^{\text{cs}}(x_j, y_j). \tag{8}$$

3 DOWNWASH OPTIMISATION FRAMEWORK

A framework, shown in Figure 4, has been developed to apply the novel B-spline movable formulation inside an optimisation process, where the inputs are the wing planform, a grid with the x and y locations of the control points, the flight points and the objective for which the movable downwash distribution is determined.

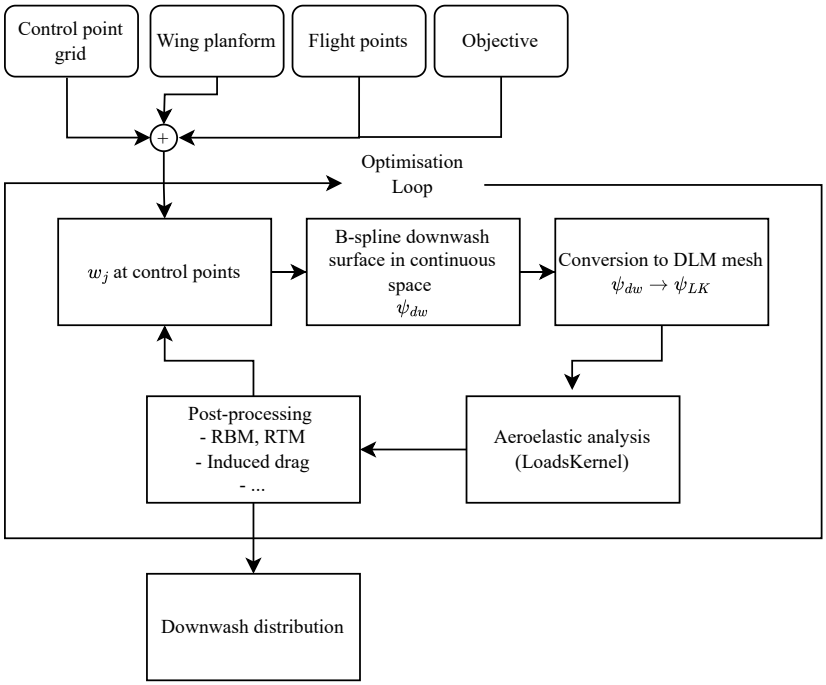

Figure 4: Downwash distribution optimisation toolchain

The inputs are imported into the optimisation process, which has been created using openMDAO [34], where, as a first step, the downwash value at the control points is specified, and the downwash distribution is generated, for which the NURBS-Python package developed by Bingol and Krishnamurthy [33] is used. After the downwash distribution has been generated, the optimisation process maps the downwash distribution to the DLM panels using equation (8), with the corresponding downwash at each panel serving as an input for the aeroelastic analysis.

For the aeroelastic analysis, the open-source code Loads Kernel – which has been developed at DLR Institute of Aeroelasticity and allows for the calculation of quasi-steady and dynamic manoeuvre loads, unsteady gust loads in the time and frequency domain, and dynamic landing loads based on a generic landing gear module [27, 35] – is used.

The final step in optimisation is extracting the loads at the preselected locations of interest and the global aerodynamic properties, such as the induced drag coefficient. The optimiser uses the extracted values to update the downwash value at the control points used to generate the downwash distribution, with the loop continuing until the optimiser reaches a minimum value of the objective function, with the output being the downwash distribution from which the movable layout can be deduced.

To perform the optimisation, the IPOPT optimiser embedded in the openMDAO PyOptSparse driver is used [36–38]. IPOPT implements an interior point line search filter to find a local solution to a nonlinear problem [38]. Inside the optimisation framework, an initial guess of

zero downwash at all control points was applied, such that the optimiser started from a clean wing to make sure the optimised downwash distribution could be achieved from the optimal cruise shape.

4 DESIGN PROBLEM

In this section, the design problem is presented. First, the aircraft model and flight point are discussed, followed by the movable definition to which the continuous parameterisation is applied. The movable definition is followed by the definition of the objective function and the constraints, with the section closing with a summary of the optimisation problem formulation.

4.1 Aircraft model

The aircraft model used throughout the analysis is based on the U-HARWARD, which is an Ultra High Aspect Ratio Wing (UHARW) aircraft with a passenger capacity and range similar to a single-aisle aircraft [21,22]. In line with WP2.2 of the UPWing project, a dry-wing concept on a fully loaded aircraft is investigated. During the optimisation process, one single flight point at an altitude of FL330, approximately 10 km, and a Mach number M = 0.75 is considered.

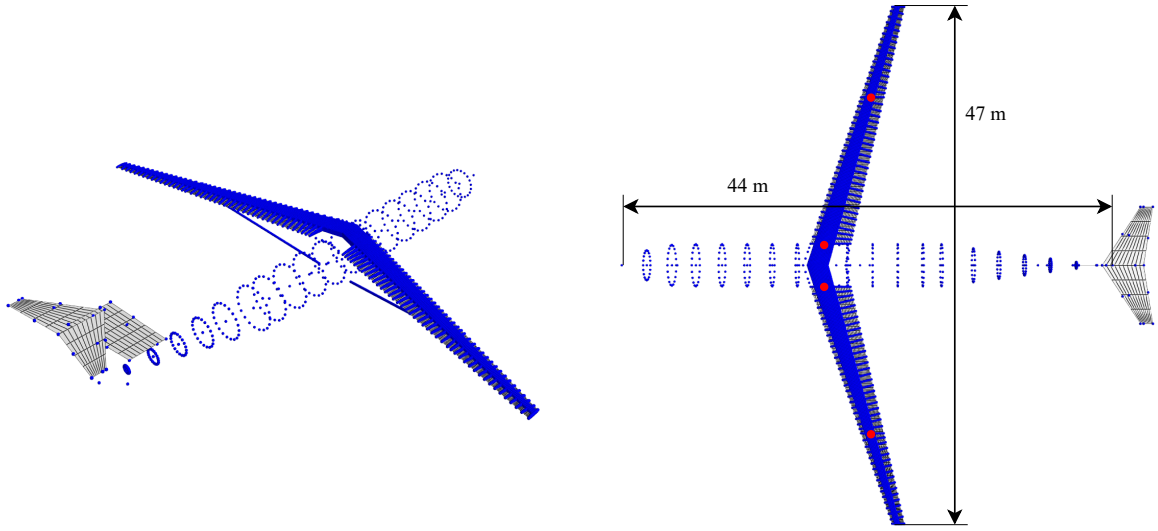

(a) Isometric view of aircraft model

(b) Basic dimensions of aircraft model

Figure 5: U-HARWARD aircraft model [22]. The structure is blue, the DLM mesh is grey, and the red dots indicate the load extraction points. Inboard dots: Wing root; Outboard dots: Wing-strut intersection

An overview of the U-HARWARD model, shown in Figure 5, where the structure is shown in blue, the DLM panels are shown in grey, and the red dots indicate the location of interest for the loads. The aerodynamic mesh consists of two wing halves, with no panels above the fuselage, a vertical tailplane (VTP) with a rudder and a movable horizontal tailplane (HTP). Each half-wing contains 54 spanwise and 25 chordwise DLM panels, leading to 2700 wing panels. The HTP contains ten chordwise panels and eight spanwise panels, whereas the VTP consists of five spanwise and ten chordwise panels. Therefore, the total aircraft model consists of 2830 DLM panels, which are used to determine the aerodynamic loads. Eight reduced frequencies were used to determine the unsteady AIC necessary for the roll simulation, after which rational function approximation (RFA) was performed to convert the unsteady AIC from frequency to time domain. For the structural part, the first ten flexible modes were considered.

4.2 Movable definition

Two different movable parameterisations are analysed to compare the novel B-spline movable definition with a more conventional discrete definition. The reference movable parameterisation, shown on the left wing in Figure 6, is based on the SUGAR Transonic-Truss-Braced-Wing aircraft [39, 40] which has a planform and performance requirements that are similar to the U-HARWARD aircraft model and consists of four ailerons and six flaps. In the case of symmetric manoeuvres, the reference movable parameterisation can use the flaps and ailerons, whereas, during an asymmetric manoeuvre such as roll, the reference parameterisation can only use the ailerons. The region the continuous formulation can influence is independent of the type of manoeuvre and is shown on the right wing, which has the same chordwise fraction and spanwise extent as the reference parameterisation.

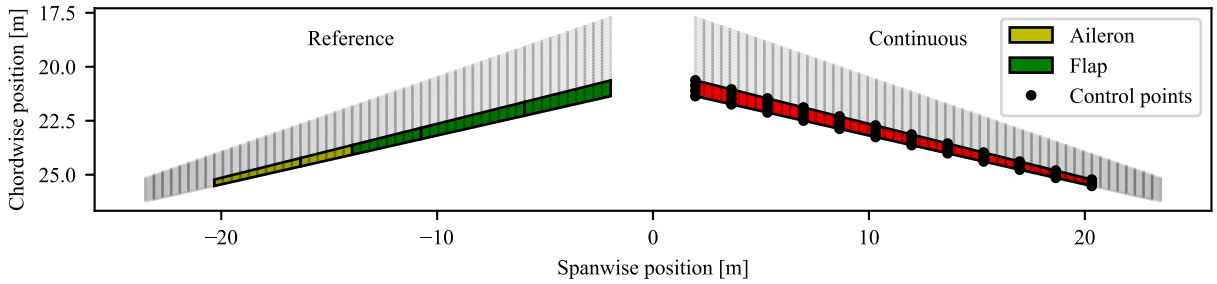

Figure 6: Left: Reference movable parameterisation. Based on SUGAR Transonic-Truss-Braced-Wing [39, 40]. Right: Movable region influenced by B-spline formulation

Figure 6 also indicates the positions of the available control points. Inside each region, the control points are spaced equally along the span and chord. As continuous movables can form reflex aerofoils, the modelling and optimisation must consider this behaviour. Figure 3 showed that a minimum of four control points are necessary to model the reflex aerofoil behaviour. Hence, four control points are used in a chordwise direction at each spanwise position. The 12 spanwise positions inside each region ensure that the downwash distribution can model spanwise morphing of the trailing edge.

4.3 Objective function

In this paper, two objective functions, V_i, are considered. The first is related to load alleviation of the wing loads during pull-up manoeuvres (manoeuvre load alleviation (MLA)), and the second minimises the induced drag coefficient to improve cruise performance for multiple different mass configurations.

For MLA, the goal is to decrease the maximum loads, $\mathbf{P}_c$, seen during the manoeuvres. Because one of the main driving factors for the structural weight of the wing is the bending moment M_x [7, 41], the first objective function is defined as:

$$V_1 = M_{x,c} \tag{9}$$

where the bending moment $M_{x,c}$ is minimised at one of the four locations of interest, indicated by the red dots in Figure 5b. The subscript c indicates which location is considered. In the case of symmetric manoeuvres, the locations on the left and right-wing have the same absolute value of the bending moment; hence, only the locations on one half-wing need to be considered, whereas, in the case of an asymmetric manoeuvre, all four locations are to be considered.

The second objective function optimises the cruise performance of the aircraft through a minimisation of the induced drag coefficient $C_{d,\text{ind}}$, which leads to the following objective function:

$$V_2 = C_{d,\text{ind}}. \tag{10}$$

4.4 Constraints

This section presents the different constraints applied to the optimisation problem. First, the limit loads necessary to determine the load envelope are discussed, which is followed by the constraints on the movable deflections. The section is closed off by discussing the handling quality and angle of attack constraints.

Limit Loads

The deflection of movables to reduce the loads or improve the aerodynamic performance may lead to additional loads applied to the aircraft, e.g., the control surface hinges. Hence, it is necessary to ensure that the loads seen by the plane during the movable deflection do not exceed the aircraft structure's limit loads at any point, with this constraint causing the downwash applied at the control points to be reduced, with the most aggressive types of lift redistribution not being possible. Hence, the first constraint can be formulated as follows:

$$C_1 : \mathbf{P}_{\text{c, lower}} \leq \mathbf{P}_c \leq \mathbf{P}_{\text{c, upper}} \tag{11}$$

Where the subscript c indicates the relevant loads at locations of interest throughout the aircraft, examples are the bending moment M_x and shear force F_z at the wing root and the wing-strut intersection.

To determine the limit loads, extreme manoeuvres are simulated using representative steady trim cases. An overview of the manoeuvres used to compute the limit loads, which have been inspired by Pusch et al. [7] and is shown in Table 1, where the question marks indicate the parameters (q: pitch rate, η: elevator deflection and ξ : aileron deflection) which are solved to match the given load factor n_z and roll rate p.

Table 1: Trim table with manoeuvres used to compute limit loads. Manoeuvres taken from Pusch et al. [7]

ID	Name	n_z	p	q	η	ξ
M0	Level flight	1	0	0	?	0
M1a	Push-over	-1 g	0	?	?	0
M1b	Pull-up	2.5 g	0	?	?	0
M2a	Roll and push	0	$\pm 15\,°/\text{s}$	?	?	?
M2b	Roll and pull	$\frac{2}{3} \cdot 2.5$ g	$\pm 15\,°/\text{s}$	?	?	?

Movable deflection angle

The allowable downwash value at the control points must be limited to prevent unrealistic deflection angles and consider actuator limitations, with equation (5) showing that the main driver behind the downwash value seen by the panels is the deflection angle u_x.

Therefore, the limits for the downwash value at a single control point are based on the downwash seen by the movable region when it is deflected as a discrete movable. For the inboard regions, up to 65 % of the semi-span, the deflection angle ranges between 5° trailing edge up and 20° trailing edge down, as this region must show a flap-like behaviour. For the outboard regions, the

deflections range between $\pm 15°$. The deflection limits were introduced because DLM cannot account for flow separation. The split between the inboard and outboard regions was set at 65 %, where the strut attaches to the wing of the U-HARWARD model. For the regions shown in Figure 6, the downwash limits correspond to

$$\begin{aligned} \xi_{\text{inboard, min}} &: w_j = -0.08 \\ \xi_{\text{inboard, max}} &: w_j = 0.3 \\ \xi_{\text{outboard, min}} &: w_j = -0.25 \\ \xi_{\text{outboard, max}} &: w_j = 0.25 \end{aligned} \tag{12}$$

Furthermore, the aircraft also needs to be trimmed during the manoeuvres. Hence, the elevator deflection angle η is also considered, with the deflection angle ranging between $\pm 15°$.

Therefore, the second constraint can be formulated as

$$C_2 : \begin{cases} -0.25 \leq w_{j,\text{out}}^{CP} \leq 0.25 \\ -0.08 \leq w_{j,\text{in}}^{CP} \leq 0.3 \\ -15° \leq \eta \leq 15° \end{cases} \tag{13}$$

Handling qualities

As the wing movables are also used to control the aircraft laterally, lateral manoeuvrability must be maintained. Regulations describe roll performance as the time necessary to accomplish a bank angle reversal. In general, by specifying an achievable steady-state roll rate (p_{max}) of 15 °/s, the handling quality requirements are fulfilled; therefore, the constraint can be written as

$$C_3 : p \geq p_{\text{max}}. \tag{14}$$

The specification of an achievable steady-state roll rate is similar to the approach used by Pusch et al. [7]. However, as mentioned by Pusch et al. and Sadraey, roll acceleration depends on actuator dynamics and mass moment of intertia [7,41], which in this case are assumed not to be affected. Hence, no further handling quality constraints are considered.

Angle of Attack

As the DLM method does not consider flow separation, the range of angle of attack (AoA) available to the optimiser needs to be limited, with the limits being $\pm 10°$.

$$C_4 : \text{AoA}_{\text{min}} \leq \text{AoA} \leq \text{AoA}_{\text{max}} \tag{15}$$

4.5 Optimisation Problem Formulation

Finally, the optimisation problem can be formulated as

$$\min_{\mathbf{D}_{\text{CP}}} (V_i) \quad \text{s.t.} \quad C_1 ... C_4 \quad \text{are satisfied.} \tag{16}$$

In equation (16), V_i is the objective function described in Section 4.3 and the constraints $C_1 ... C_4$, presented in Section 4.4. An overview of the values of the constraints is given in Table 2. The

Table 2: Constraint overview

ID	Value
C_1 *	$\mathbf{P}_{\text{c, lower}} \leq \mathbf{P}_c \leq \mathbf{P}_{\text{c, upper}}$
C_2^a †	$\begin{cases} -0.25 \leq w_{j,\text{out}}^{CP} \leq 0.25 \\ -0.08 \leq w_{j,\text{in}}^{CP} \leq 0.3 \\ -15^\circ \leq \eta \leq 15^\circ \end{cases}$
C_2^s ‡	$\begin{cases} -0.25 \leq w_{j,\text{out}}^{CP} \leq 0.25 \\ -0.08 \leq w_{j,\text{in}}^{CP} \leq 0.3 \\ -15^\circ \leq \eta \leq 15^\circ \end{cases}$
C_3	$p \geq 15\,^\circ/\text{s}$
C_4	$-10^\circ \leq \text{AoA} \leq 10^\circ$

* Limit loads: $-3.71 \times 10^5\,\text{N} \leq F_{z,\text{wing-strut}} \leq 1.41 \times 10^5\,\text{N}$; $-3.36 \times 10^6\,\text{N m} \leq M_{x,\text{wing-strut}} \leq 9.62 \times 10^6\,\text{N m}$; $-8.24 \times 10^5\,\text{N} \leq F_{z,\text{root}} \leq 3.72 \times 10^5\,\text{N}$; $-9.62 \times 10^6\,\text{N m} \leq M_{x,\text{root}} \leq 3.36 \times 10^6\,\text{N m}$

† Constraint C_2 for asymmetric manoeuvres. Constraint C_3 is included by specifying the roll rate during the manoeuvre.

‡ Constraint C_2 for symmetric manoeuvres. Constraint C_3 is included through an update of w_j limits.

available design parameters are the downwash values at the control points $\mathbf{D}_{\text{CP}}$ described in Section 2.2.

To ensure that the aircraft can always perform a roll, several steps must be taken during the optimisation process. In the case of a symmetric manoeuvre such as a 2.5 g pull-up manoeuvre or cruise performance optimisation, first, the downwash distribution required to satisfy constraint C_3 is determined, after which the required downwash distribution is subtracted from C_2 to create C_2^s, which contains the updated budgets for symmetric manoeuvres. An example of this step is given for control point a in the equation below.

$$-0.25 - \min\left(w_{j,\text{a, roll}}\right) \leq w_{j,\text{a}}^{CP} \leq 0.25 - \max\left(w_{j,\text{a, roll}}\right) \tag{17}$$

For the manoeuvre M2b, MLA applied during roll, the above step is unnecessary, as the optimiser already needs to satisfy the roll constraint C_3.

5 RESULTS

The results obtained using the optimisation problem described in the previous section are presented in this section. First, the roll analysis results are discussed, followed by load alleviation results for a 2.5 g pull-up manoeuvre. The final results are related to optimising objective function V_2, which minimises the induced drag coefficient.

5.1 Handling Qualities: Roll

The roll results are split into two main sections; the first results are for the pure roll analysis required as input for the pull-up manoeuvre and cruise performance optimisation. The second is for the roll and pull manoeuvre, where MLA is applied during roll manoeuvres.

Comparing the downwash distribution for a pure roll in Figure 7, it can be seen that the reference movable parameterisation uses both the inboard and outboard ailerons, but the right-wing ailerons provide a larger contribution to the rolling moment, which can be seen in Figure 8. Furthermore, it can also be seen that the main contribution towards the roll comes from the outboard

ailerons, which have the largest moment arm and the largest physical size. The continuous parameterisation uses the entire outboard region in an equal amount, with the lift distribution due to applied downwash being equal in magnitude but opposite in sign on the left and right wings. However, in the downwash and lift distributions, it can be seen that the equivalent moment arm of the continuous parameterisation on the left and right wings (LW, RW) are more similar – LW: 16.7 m; RW: 16.6 m – than those of the reference parameterisation – LW: 17.2 m; RW: 16.8 m – which explains the lower downwash level required by the continuous parameterisation, and the higher downwash level on the right wing of the reference parameterisation.

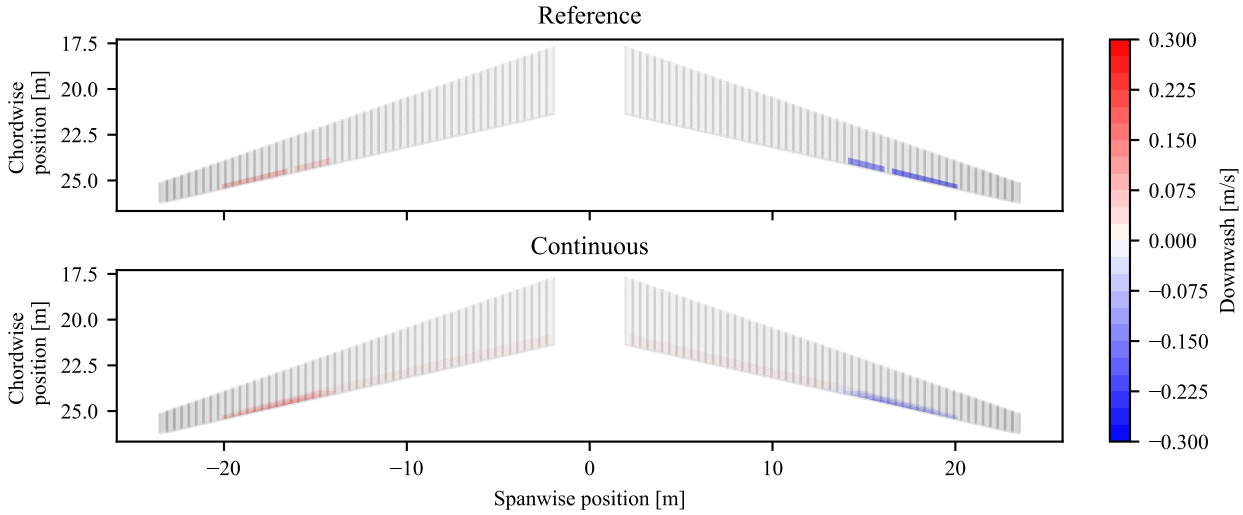

Figure 7: Downwash distribution for 15 °/s roll

Similar behaviour in the downwash and load distribution can be seen when the reference and continuous parameterisation are compared. The root bending moment at the left and right root, presented in Table 3, show a difference of 1.3×10^4 N m for the left root and 9×10^4 N m for the right root when comparing the reference and continuous parameterisation, hence, the effect of the reference and continuous parameterisation is seen as equivalent.

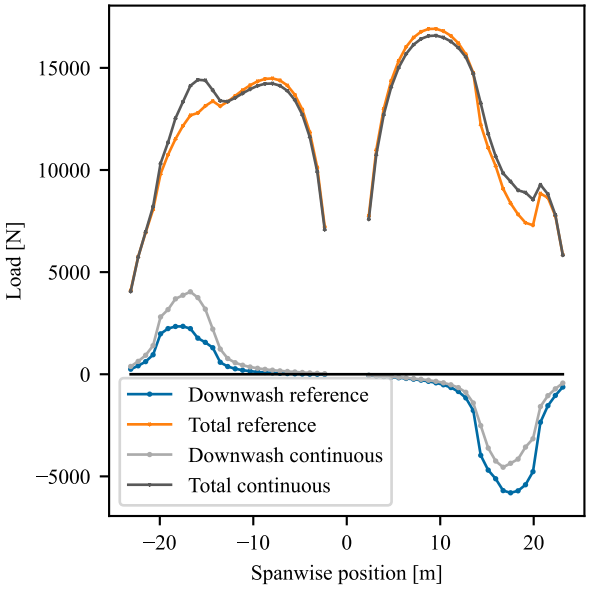

Figure 8: Lift distribution for 15 °/s roll

The second set of results presented in this section are the results related to MLA during the roll and pull-up manoeuvre (M2b). The objective function V_1 is modified to allow the inclusion of two load extraction locations at the wing root, with $V_1 = \text{abs}(M_{x,\text{left root}}) + \text{abs}(M_{x,\text{right root}})$ used during the minimisation of the root bending moments during the roll and pull-up manoeuvre.

The downwash distribution, shown in Figure 9, shows that both the reference and continuous parameterisation show a similar downwash distribution, with a negative downwash applied on the right wing, which is used to reduce the bending moment at the root and generate the required rolling moment for the right roll. Furthermore, on the left wing, both positive and negative downwash are applied, with the positive downwash being used to generate the rolling moment – also shown by the lift distribution in Figure 10 – and the negative downwash used to redistribute the lift and reduce the bending moments at the wing roots. The inboard section of the continuous distribution on the left and right wings in Figure 9 shows a small amount of applied downwash – causing a positive load on the left wing and a negative load on the right wing – with this downwash used to generate the roll and reduce the root bending moments, as such behaviour was not seen in the downwash distribution for a pure roll in Figure 7. Figure 9 also show that on the inboard section of the left wing, close to the root, a negative downwash is applied, which causes a negative load that is also used to reduce the bending moments. Furthermore, in Figure 9, it can be seen that the outboard region of the left wing of the continuous parameterisation shows reflex behaviour, which is used to reduce the root bending moments further.

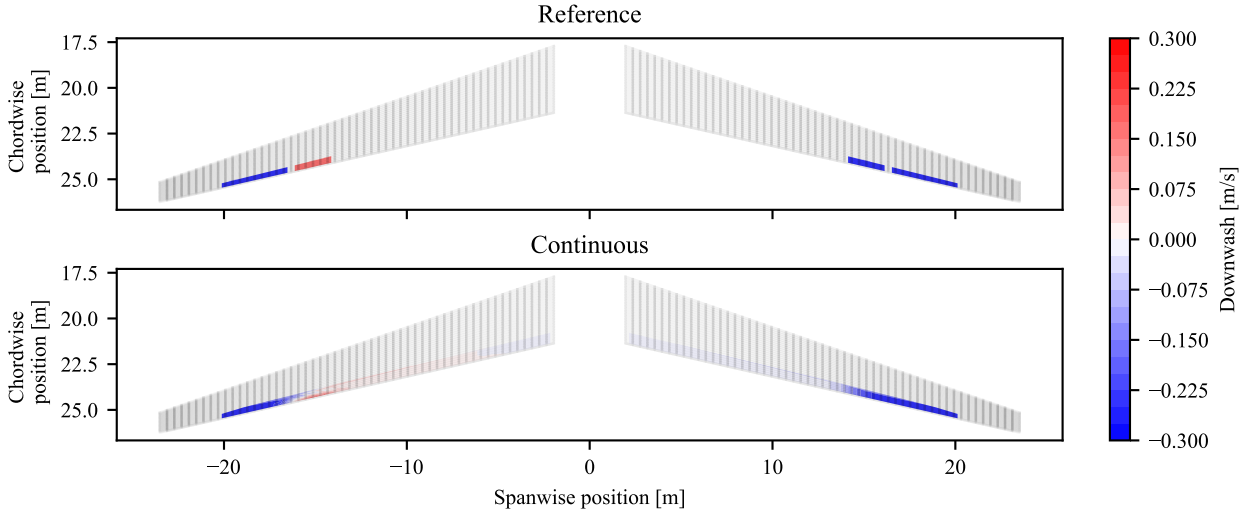

Figure 9: Downwash distribution for 15 °/s roll with MLA

The lift distributions for the reference and continuous parameterisations in Figure 10 show comparable lift distributions. The main differences are the reduced positive downwash load of the continuous parameterisation at the location of the inboard aileron, which is caused by the ability of the continuous parameterisation to use the full TE, and the increased negative load on the inboard section of the right-wing – also shown by the lower peak value of the total lift of the continuous parameterisation.

Comparing the bending moment and shear force results at the roots in Table 3, one can see that MLA applied during a right roll reduces the bending moments and shear forces at the root monitoring stations. The reference parameterisation can reduce the root bending moment by 7.14×10^5 N m on the left root and 2.80×10^5 N m when compared to a pure roll at 15 °/s,

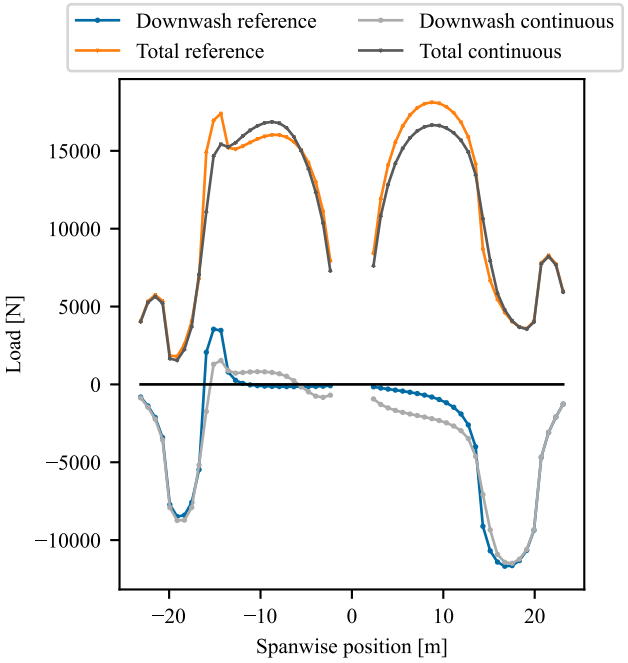

Figure 10: Lift distribution for 15 °/s roll with MLA

whereas the continuous parameterisation reduces the bending moment by 9.4×10^5 N m at the left root and 3.7×10^5 N m at the right root.

Table 3 also shows that during a pure roll, the reference parameterisation generates a lower bending moment at the wing roots; the continuous parameterisation can reduce the bending moment to a lower value. Furthermore, the bending moments at the right-wing root with MLA applied reach a value of 1.78×10^6 N m for the reference and continuous parameterisation. This is because the aircraft is in a right roll, and part of the downwash budget is used to achieve the 15 °/s roll, with the downwash distribution in Figure 9 showing the same downwash values applied on the right wing in the outboard region, which means a similar lift distribution – see Figure 10 – leading to the same bending moment at the right root.

However, using the continuous downwash distributions in Figures 7 and 9, it can be concluded that the reference and continuous parameterisation show similar downwash distributions, meaning that the novel continuous movable parameterisation can determine a movable layout with only the wing planform and a set of flight points is known.

Table 3: Bending moments and shear forces at root monitoring stations during roll

	Left wing root		Right wing root	
	M_x [N m]	F_z [N]	M_x [N m]	F_z [N]
Reference	-2.04×10^6	2.37×10^5	2.06×10^6	2.46×10^5
Continuous	-2.17×10^6	2.39×10^5	2.15×10^6	2.48×10^5
abs (ΔLoads)	1.30×10^4	2.00×10^3	9.00×10^4	2.00×10^3
Reference MLA	-1.29×10^6	2.35×10^5	1.78×10^6	2.35×10^5
abs (ΔLoads Reference)	7.50×10^5	2.00×10^3	2.80×10^5	1.10×10^4
Continuous MLA	-1.23×10^6	2.37×10^5	1.78×10^6	2.26×10^5
abs (ΔLoads Continuous)	9.40×10^5	2.00×10^3	3.70×10^5	2.20×10^4

5.2 Manoeuvre Load Alleviation

This section presents the MLA results for a 2.5 g pull-up manoeuvre at two different load extraction positions. Figures 11 and 12, which present the lift and downwash distribution, show the final results of MLA applied to the wing root, with Figures 13 and 14 showing the results at the wing-strut attachment.

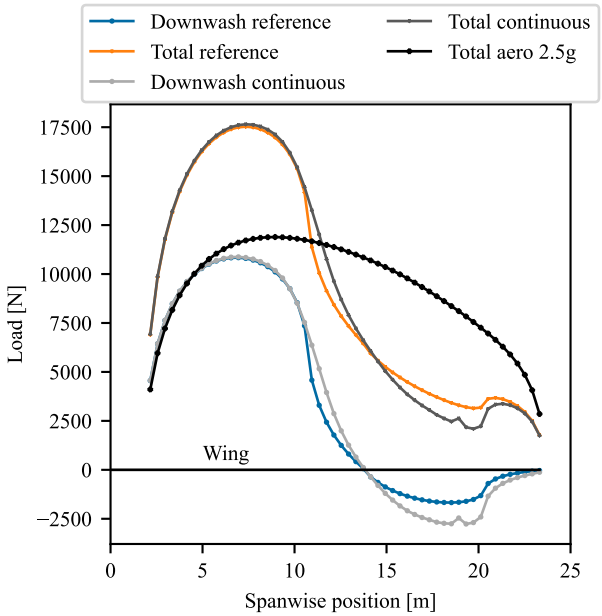

Figure 11: Lift distribution for min (M_x) at the root during a 2.5 g pull-up

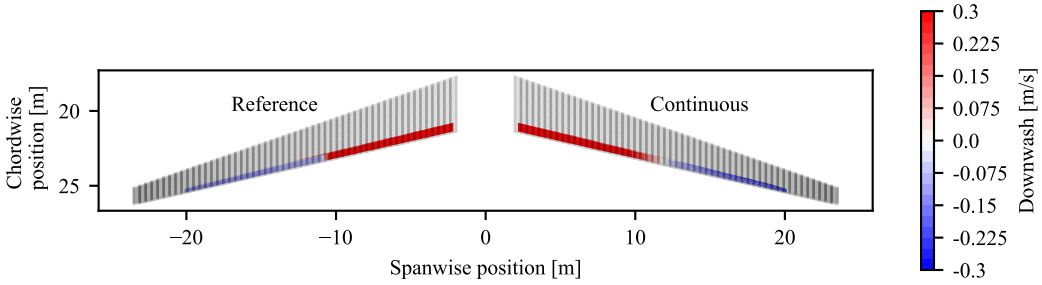

Figure 12: Downwash distribution for min (M_x) at the root during a 2.5 g pull-up

A comparison of the different bending moments, M_x, and shear force F_z at the load extraction positions per half-wing are shown in Table 4, which first presents the bending moments and shear forces for a clean wing experiencing a 2.5 g pull-up manoeuvre, after which, the different MLA results are presented. First, the MLA results with V_1 applied to the root are presented, which are followed by the results where V_1 is applied to the wing-strut intersection.

When the lift distributions in Figures 11 and 13 are compared, distinct differences can be seen. For example, for the root bending minimisation, the lift is redistributed over a more extensive section of the wing when compared to the wing-strut bending moment minimisation. The wing-root results show a load which is larger in magnitude on the inboard section of the wing, approximately 17 500 N when compared to the wing-strut MLA results, whose peak is around 15 000 N. These differences are as expected, as the aircraft is trimmed for a 2.5 g pull-up and the equivalent moment arm for the root is smallest for the wing-root MLA results, which causes the wing-root bending moments to be reduced further than when the wing-strut MLA case is

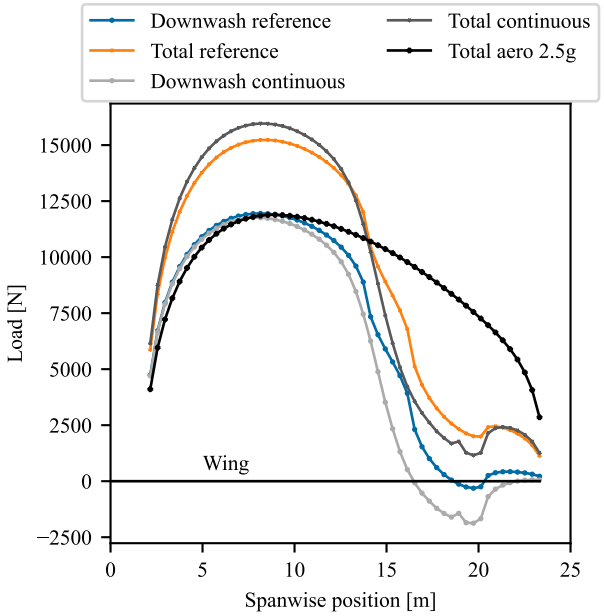

Figure 13: Lift distribution for min (M_x) at the wing-strut attachment location during a 2.5 g pull-up

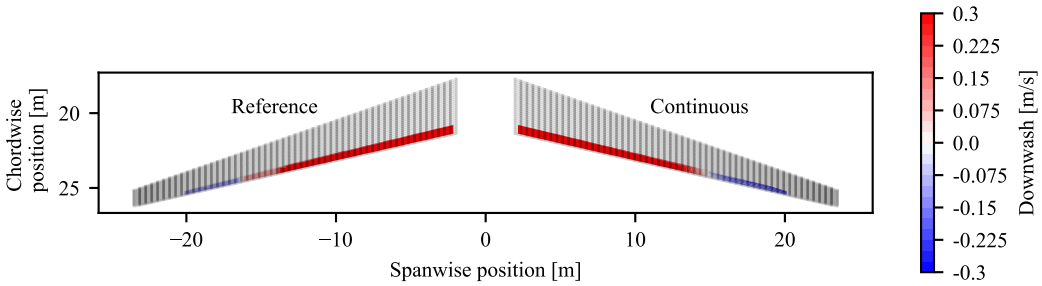

Figure 14: Downwash distribution for min (M_x) at the wing-strut attachment location during a 2.5 g pull-up

considered.

The bending moment and shear forces at the different monitoring stations in Table 4 show that both the wing-strut and wing-root MLA cases can reduce the bending moments at all locations of interest. This is also expected, as the lift for both MLA cases is redistributed to reduce the bending moments. Comparing the results for the reference and continuous parameterisation in Table 4, the continuous parameterisation can reduce the root bending moment by a maximum of 1.4×10^6 N m, whereas the reference parameterisation reduced the root bending moment by a maximum of 1.3×10^6 N m. A similar trend is seen for the wing-strut intersection, where the continuous parameterisation reduced the bending moment by a maximum of 3.7×10^5 N m, and the reference parameterisation reduced it by a maximum of 3.4×10^5 N m.

The ability of the continuous parameterisation to reduce the bending moment further when compared to the reference parameterisation is caused by the ability of the continuous parameterisation to apply more downward load in the outboard region, which comes from the larger downwash budget which is available based on the roll analyses that are included in the C_2^s constraint.

However, when comparing the downwash distribution in Figures 12 and 14, it can be seen that the reference and continuous parameterisation tend towards the same type of downwash distri-

Table 4: Bending moments and shear forces at monitoring stations during a 2.5 g pull-up manoeuvre

	Wing-strut intersection		Wing root	
	abs (M_x) [N m]	F_z [N]	abs (M_x) [N m]	F_z [N]
Clean wing	5.05×10^5	1.42×10^5	3.36×10^6	3.72×10^5
Reference root MLA	2.38×10^5	5.82×10^4	2.06×10^6	3.62×10^5
Continuous root MLA	2.01×10^5	4.63×10^4	1.96×10^6	3.61×10^5
Reference wing-strut MLA	1.63×10^5	5.33×10^4	2.32×10^6	3.69×10^5
Continuous wing-strut MLA	1.35×10^5	3.64×10^4	2.13×10^6	3.66×10^5

bution. Hence, the novel continuous movable parameterisation allows for the determination of a movable layout which can be used for MLA, where roll constraints are included when only the wing planform is known.

5.3 Cruise Performance: Induced Drag

This section presents the results for the objective function V_2. Five mass cases have been considered for the induced drag analysis, with Table 5 giving an overview of the different mass cases. The mass cases range from an aircraft at maximum takeoff weight, MTOW (M1), through different fuel masses (M2 ... M4) to an aircraft with no fuel onboard (M5).

Table 5: Mass cases considered for induced drag coefficient analysis

ID	Mass components
M1	Aircraft + payload + 100 % fuel
M2	Aircraft + payload + 75 % fuel
M3	Aircraft + payload + 50 % fuel
M4	Aircraft + payload + 25 % fuel
M5	Aircraft + payload

The values for $C_{d,\text{ind}}$ for different mass cases are presented in Table 6, and Figure 15 shows the change of $C_{d,\text{ind}}$ using the lift-to-induced-drag-ratio $C_l/C_{d,\text{ind}}$ to remove the effect of reduction in the required lift at lighter mass cases. Both Table 6 and Figure 15 show that induced drag reduces with a decrease in mass, which is as expected, as less lift needs to be generated; however, it can be seen that the movables can reduce the induced drag coefficient, with the reference parameterisation reducing $C_{d,\text{ind}}$ by 1.6 %, whereas the continuous movable parameterisation reduces $C_{d,\text{ind}}$ by 4 % on average. The trends in the $C_l/C_{d,\text{ind}}$ ratio show that the induced drag coefficient is reduced more than the required lift is reduced, and therefore improving aircraft performance, with Table 6 showing that when the aircraft becomes lighter, the reduction in the induced drag coefficient becomes bigger on a percentage basis – also shown in the increasing gap between the different configurations in Figure 15. The reductions in the induced drag coefficient will allow for a reduced fuel burn or an increased payload for the same fuel burn. The entire flight mission must be studied to determine the full benefits of using the movables to reduce the induced drag coefficient, such that all design and off-design cases are included.

The lift and downwash distribution for mass case M5, as depicted in Figures 16 and 17, show that both movable parameterisations apply a downward load to create an elliptical lift distribution on each half-wing. Comparing the optimised lift distributions to the clean wing, it can be seen that the centre of pressure of the half-wing is moved more outboard, allowing for a lift distribution which resembles an elliptical lift distribution more closely.

Table 6: Induced drag coefficients for different mass cases. % Difference is shown with respect to clean wing

ID	Clean wing	Reference	% Difference	Continuous	% Difference
M1	1.13×10^{-2}	1.11×10^{-2}	−1.6	1.09×10^{-2}	−3.2
M2	8.90×10^{-3}	8.76×10^{-3}	−1.6	8.58×10^{-3}	−3.7
M3	6.82×10^{-3}	6.71×10^{-3}	−1.6	6.55×10^{-3}	−3.9
M4	5.02×10^{-3}	4.94×10^{-3}	−1.6	4.80×10^{-3}	−4.4
M5	3.49×10^{-3}	3.43×10^{-3}	−1.7	3.33×10^{-3}	−4.7

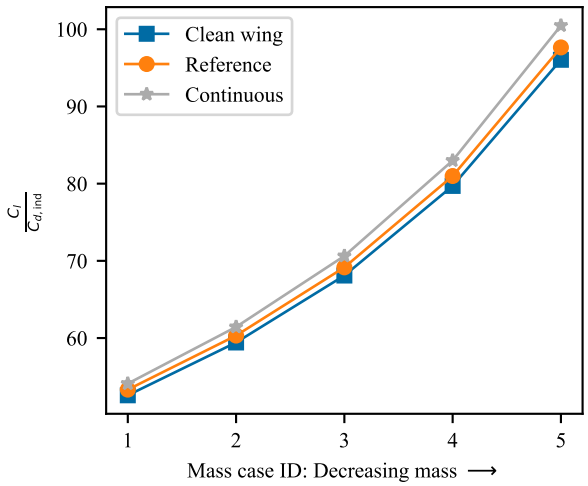

Figure 15: Comparison of $C_l/C_{d,\mathrm{ind}}$ for different mass cases

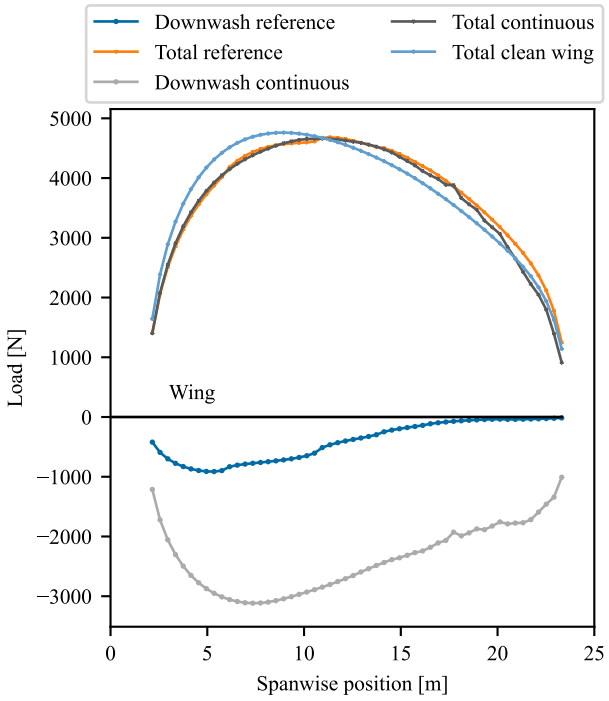

Figure 16: Lift distribution for mass case M5

Comparing the downwash distributions in Figure 17, it can also be seen that the reference parameterisation only uses the flaps, whereas the continuous parameterisation also uses the aileron region. Furthermore, the effect of the reflex aerofoil behaviour, which is allowed by the continuous parameterisation, can also be seen, as the continuous parameterisation shows different

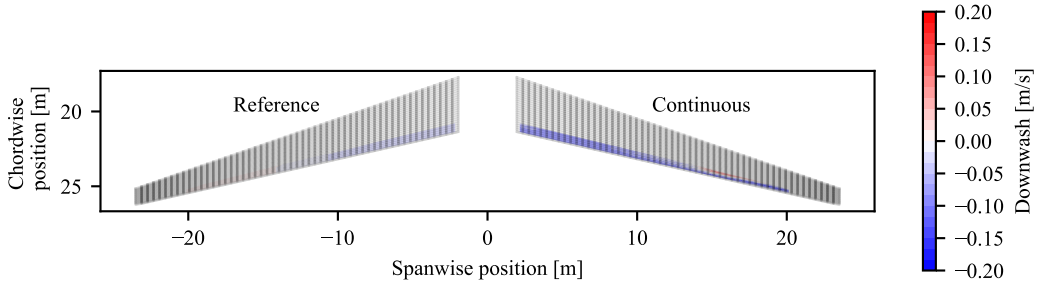

Figure 17: Downwash distribution for mass case M5

downwash levels in the chordwise direction. The required reflex behaviour in the aileron region can only be achieved by continuous parameterisation. Hence, the reference parameterisation does not use the ailerons, as it cannot achieve the required downwash distribution using the reference movable parameterisation.

However, even though the reference and continuous parameterisations show differences in the downwash distribution, for example, the amount of downwash which can be applied and the reflex behaviour in the downwash distribution, it can be concluded that the continuous formulation allows for the determination of a movable layout that is similar to the reference.

6 CONCLUSION

This paper has shown a novel parameterisation methodology for movables, which uses a direct assignment of the downwash to the DLM panels to model different movable layouts. The parameterisation methodology was applied to the U-HARWARD aircraft model, and the aircraft performance was assessed for roll capability, manoeuvre load alleviation (MLA) and cruise performance. For comparison, the continuous parameterisation was applied to the same spanwise and chordwise extent as a reference parameterisation consisting of ailerons and flaps.

The results in the paper show that using the same set of constraints, the continuous parameterisation can determine a downwash distribution which is at least equal in performance, for example, during pure roll or has better performance – for MLA and cruise performance – than the reference parameterisation. For example, the reference parameterisation can reduce the root bending moment (RBM) by 38 %. In contrast, the continuous parameterisation reduces the RBM by 41 %, showing a 3 percentage points improvement over the reference parameterisation Furthermore, for the induced drag coefficient, the continuous parameterisation reduces $C_{d,\text{ind}}$ by 4 % on average, with the reference parameterisation only reducing $C_{d,\text{ind}}$ 1.6 %, which shows that the continuous parameterisation can reduce the induced drag coefficient by 2.4 percentage points more than the reference parameterisation.

Further work is required in the steps needed to convert from the optimised downwash distribution to a movable layout and corresponding deflections. Another aspect that needs to be investigated is the automatic model generation of the aeroelastic model, such that different aircraft planforms can be investigated based on typical parameters such as the span, aspect ratio, and sweep angle. In line with this, implementing the ability to determine the gradients required by the optimiser using multiprocessing would be beneficial to speed up the optimisation process; however, it requires changes to the implementation of the aeroelastic solver. Finally, the current parameterisation only considers flap-like and aileron-like movables on the trailing edge. The ability to include additional types of control surfaces, such as spoilers, in the downwash distribution is expected to bring further improvements.

To conclude this section, the presented results have demonstrated the successful application of a movable parameterisation methodology, which can be applied to an aircraft for which only the planform and initial structural parameters are known and which can be applied to explore the design space available for the wing movables.

ACKNOWLEDGEMENTS

The work presented herein has been partially funded by the European Community's Clean Aviation programme under the Grant Agreement 101101974. The UPWing project (Ultra-Performance Wing) is a project funded under the topic Climate, Energy and Mobility, involving 26 partners. The project started on January 1, 2023.

The U-HARWARD configuration has been used as the baseline configuration in the UPWing project. The authors would like to thank ONERA for providing the U-HARWARD model.

7 REFERENCES

[1] Reckzeh, D. (2014). MULTIFUNCTIONAL WING MOVEABLES: DESIGN OF THE A350XWB AND THE WAY TO FUTURE CONCEPTS. In *29th Congress of the International Council of the Aeronautical Sciences (ICAS)*. St. Petersburg.

[2] Sanghi, D., Riso, C., Cesnik, C. E., et al. (2020). Impact of Control-Surface Flexibility on the Dynamic Response of Flexible Aircraft. In *AIAA Scitech 2020 Forum*, AIAA SciTech Forum. American Institute of Aeronautics and Astronautics. doi:10.2514/6.2020-1185.

[3] Sanghi, D., Riso, C., Cesnik, C., et al. (2020). Influence of Aileron Placement on Roll Response of High-Aspect-Ratio-Wing Aircraft. In *AIAA AVIATION 2020 FORUM*, AIAA AVIATION Forum. American Institute of Aeronautics and Astronautics. doi:10.2514/6.2020-2645.

[4] Sanghi, D. (2022). *Maneuverability, Load Alleviation, and Ride Qualities of Transonic High-Aspect-Ratio-Wing Aircraft*. Ph.D. thesis, University of Michigan. doi:10.7302/6868.

[5] Riso, C., Sanghi, D., Cesnik, C. E., et al. (2020). Parametric Roll Maneuverability Analysis of a High-Aspect-Ratio-Wing Civil Transport Aircraft. In *AIAA Scitech 2020 Forum*, AIAA SciTech Forum. American Institute of Aeronautics and Astronautics. doi:10.2514/6.2020-1191.

[6] Ma, Y., Abouhamzeh, M., and Elham, A. (2023). Aerostructural Optimization and Comparative Study of Strut-Braced-Wing and Twin-Fuselage Aircraft Configurations with Ultra-High Aspect Ratio Wings. In *AIAA SCITECH 2023 Forum*, AIAA SciTech Forum. American Institute of Aeronautics and Astronautics. doi:10.2514/6.2023-2204.

[7] Pusch, M., Knoblach, A., and Kier, T. (2019). Integrated optimization of control surface layout for gust load alleviation. *CEAS Aeronautical Journal*, 10(4), 1059–1069. ISSN 1869-5590. doi:10.1007/s13272-019-00367-4.

[8] Muradas Odriozola, D., Marquier, S., Morlier, J., et al. (2023). A PRELIMINARY LOW-FIDELITY MDO APPROACH FOR LOAD ALLEVIATION THROUGH MOVABLES ON HAR WING. In *Aerobest 2023*. Lisboa, Portugal: ECCOMAS, Portugal.

[9] Wunderlich, T. F. and Siebert, F. (2022). Optimization of Control Surface Deflections on the High Aspect Ratio Wing to Improve Cruise Flight Performance. In A. Dillmann, G. Heller, E. Krämer, C. Wagner, and J. Weiss (Eds.), *New Results in Numerical and Experimental Fluid Mechanics XIV*, Notes on Numerical Fluid Mechanics and Multidisciplinary Design. Cham: Springer Nature Switzerland. ISBN 978-3-031-40482-5, pp. 206–215. doi:10.1007/978-3-031-40482-5_20.

[10] Weisshaar, T. A. (2013). Morphing Aircraft Systems: Historical Perspectives and Future Challenges. *Journal of Aircraft*, 50(2), 337–353. ISSN 0021-8669. doi:10.2514/1.C031456.

[11] Mkhoyan, T. (2022). *Autonomous Smart Morphing Wing: Development, Realisation & Validation*. Ph.D. thesis, Delft University of Technology.

[12] Mkhoyan, T., Thakrar, N. R., De Breuker, R., et al. (2021). Design and Development of a Seamless Smart Morphing Wing Using Distributed Trailing Edge Camber Morphing for Active Control. In *AIAA Scitech 2021 Forum*, AIAA SciTech Forum. American Institute of Aeronautics and Astronautics. doi:10.2514/6.2021-0477.

[13] Nguyen, N., Kaul, U., Lebofsky, S., et al. (2015). Development of Variable Camber Continuous Trailing Edge Flap for Performance Adaptive Aeroelastic Wing. In *SAE AeroTech Congress & Exhibition*. Seattle, WA.

[14] Nguyen, N. T., Ting, E., Chaparro, D., et al. (2017). Multi-Objective Flight Control for Drag Minimization and Load Alleviation of High-Aspect Ratio Flexible Wing Aircraft. In *58th AIAA/ASCE/AHS/ASC Structures, Structural Dynamics, and Materials Conference*, AIAA SciTech Forum. Grapevine, Texas: American Institute of Aeronautics and Astronautics. doi:10.2514/6.2017-1589.

[15] Stanford, B. K. (2016). Static and Dynamic Aeroelastic Tailoring with Variable-Camber Control. *Journal of Guidance, Control, and Dynamics*, 39(11), 2522–2534. ISSN 0731-5090. doi:10.2514/1.G000413.

[16] De Breuker, R., Mkhoyan, T., Nazeer, N., et al. (2022). Overview of the SmartX Wing Technology Integrator. *Actuators*, 11(10), 302. ISSN 2076-0825. doi:10.3390/act11100302.

[17] Stanford, B. K. (2017). Optimal Control Surface Layout for an Aeroservoelastic Wingbox. *AIAA Journal*, 55(12), 4347–4356. ISSN 0001-1452. doi:10.2514/1.J056070.

[18] Stanford, B. K. (2020). Optimal Aircraft Control Surface Layouts for Maneuver and Gust Load Alleviation. In *AIAA Scitech 2020 Forum*, AIAA SciTech Forum. American Institute of Aeronautics and Astronautics. doi:10.2514/6.2020-0448.

[19] Binder, S., Wildschek, A., and De Breuker, R. (2019). Unsteady Aerodynamic Model Order Reduction for Aeroservoelastic Optimisation by Balanced Proper Orthogonal Decomposition and the use of Synthetic Mode Shapes. *Journal of Aeroelasticity and Structural Dynamics*, (6), 43–72. ISSN 1974-5117. doi:10.3293/asdj.2018.49.

[20] Binder, S. (2021). *Simultaneous Optimisation of Composite Wing Structures and Control Systems for Active and Passive Load Alleviation*. Ph.D. thesis, Delft University of Technology.

[21] Ricci, S., Paletta, N., Defoort, S., et al. (2022-01-03/2022-01-07). U-HARWARD: A CS2 EU funded project aiming at the Design of Ultra High Aspect Ratio Wings Aircraft. In *AIAA SCITECH 2022 Forum*. San Diego, CA & Virtual: American Institute of Aeronautics and Astronautics. doi:10.2514/6.2022-0168.

[22] Carrier, G. G., Arnoult, G., Fabbiane, N., et al. (2022-01-03/2022-01-07). Multidisciplinary analysis and design of strut-braced wing concept for medium range aircraft. In *AIAA SCITECH 2022 Forum*. San Diego, CA & Virtual: American Institute of Aeronautics and Astronautics. doi:10.2514/6.2022-0726.

[23] Torenbeek, E. (1982). *Synthesis of Subsonic Airplane Design*. Dordrecht: Springer Netherlands. ISBN 978-90-481-8273-2 978-94-017-3202-4. doi:10.1007/978-94-017-3202-4.

[24] (2018). *Aircraft Design a Conceptual Approach*. AIAA Education Series. Reston, VA: American Institute of Aeronautics and Astronautics, Inc, sixth edition ed. ISBN 978-1-62410-490-9.

[25] Werter, N. P. M., De Breuker, R., and Abdalla, M. M. (2018). Continuous-Time State-Space Unsteady Aerodynamic Modeling for Efficient Loads Analysis. *AIAA Journal*, 56(3), 905–916. ISSN 0001-1452. doi:10.2514/1.J056068.

[26] Werter, N. P. M. (2017). *Aeroelastic Modelling and Design of Aeroelastically Tailored and Morphing Wings*. Ph.D. thesis, Delft University of Technology.

[27] Voß, A. (2020). An Implementation of the Vortex Lattice and the Doublet Lattice Method. Technical Report DLR-IB-AE-GO-2020-137, Institut für Aeroelastik, Deutsches Zentrum für Luft- und Raumfahrt, Göttingen, Germany.

[28] Bertrand, X. (2008). *Modélisation aérodynamique des surfaces de contrôle de la voilure d'un avion de transport*. Ph.D. thesis, ISAE, Toulouse.

[29] Lancelot, P. and De Breuker, R. (2018-10-09/2018-10-11). Effect of improved flight and control loads modelling on wing-box preliminary sizing:. In *6th Aircraft Structural Design Conference*. Bristol, United Kingdom.

[30] Kier, T. and Looye, G. (2009-06-21/2009-06-25). Unifying Manoeuvre and Gust Loads Analysis. In *IFASD 2009*. Seattle, USA.

[31] Mkhoyan, T., Thakrar, N. R., Breuker, R. D., et al. (2022). Morphing wing design using integrated and distributed trailing edge morphing. *Smart Materials and Structures*, 31(12), 125025. ISSN 0964-1726. doi:10.1088/1361-665X/aca18b.

[32] Piegl, L. and Tiller, W. (1997). *The NURBS Book*. Monographs in Visual Communication. Berlin, Heidelberg: Springer Berlin Heidelberg. ISBN 978-3-540-61545-3 978-3-642-59223-2. doi:10.1007/978-3-642-59223-2.

[33] Bingol, O. R. and Krishnamurthy, A. (2019). NURBS-Python: An open-source object-oriented NURBS modeling framework in Python. *SoftwareX*, 9, 85–94. ISSN 2352-7110. doi:10.1016/j.softx.2018.12.005.

[34] Gray, J. S., Hwang, J. T., Martins, J. R. R. A., et al. (2019). OpenMDAO: An open-source framework for multidisciplinary design, analysis, and optimization. *Structural and Multidisciplinary Optimization*, 59(4), 1075–1104. ISSN 1615-1488. doi:10.1007/s00158-019-02211-z.

[35] Voß, A. (2021). Loads Kernel User Guide, Version 1.01. Technical Report DLR-IB-AE-GO-2020-136, Institut für Aeroelastik, Deutsches Zentrum für Luft- und Raumfahrt, Göttingen, Germany.

[36] Hwang, J. T. and Martins, J. R. (2018). A Computational Architecture for Coupling Heterogeneous Numerical Models and Computing Coupled Derivatives. *ACM Transactions on Mathematical Software*, 44(4), 37:1–37:39. ISSN 0098-3500. doi:10.1145/3182393.

[37] Wu, N., Kenway, G., Mader, C. A., et al. (2020). pyOptSparse: A Python framework for large-scale constrained nonlinear optimization of sparse systems. *Journal of Open Source Software*, 5(54), 2564. ISSN 2475-9066. doi:10.21105/joss.02564.

[38] Wächter, A. and Biegler, L. T. (2004). On the Implementation of an Interior-Point Filter Line-Search Algorithm for Large-Scale Nonlinear Programming.

[39] Harrison, N. A., Gatlin, G. M., Viken, S. A., et al. (2020). Development of an Efficient M=0.80 Transonic Truss-Braced Wing Aircraft. In *AIAA Scitech 2020 Forum*. Orlando, FL: American Institute of Aeronautics and Astronautics. ISBN 978-1-62410-595-1. doi:10.2514/6.2020-0011.

[40] Harrison, N. A., Hoffman, K., Lazzara, D. S., et al. (2023). Subsonic Ultra Green Aircraft Research: Phase IV Final Report – Volume I Mach 0.80 Transonic Truss-Braced Wing High-Speed Design Report. Technical Report NASA/CR–20220016017 Volume I.

[41] Sadraey, M. H. (2012). *Aircraft Design: A Systems Engineering Approach*. Aerospace Series (Chichester, England). Hoboken, New Jersey: Wiley. ISBN 978-1-118-35229-8.

COPYRIGHT STATEMENT